Journal of Magnetic Resonance 196 (2009) 178–190

Contents lists available at ScienceDirect

Journal of Magnetic Resonance

journal homepage: www.elsevier.com/locate/jmr

Distributions of transverse relaxation times for soft-solids measured in strongly inhomogeneous magnetic fields

R.I. Chelcea [a], R. Fechete [a,*], E. Culea [a], D.E. Demco [a,c], B. Blümich [b,*]

[a] Technical University of Cluj-Napoca, Daicoviciu 1, R-400020 Cluj-Napoca, Romania
[b] Institut für Technische und Makromolekulare Chemie, RWTH-Aachen University, Worringerweg 1, D-52056 Aachen, Germany
[c] DWI an der RWTH-Aachen University e.V. Pauwelsstr. 8, D-52056 Aachen, Germany

ARTICLE INFO

Article history:
Received 29 September 2008
Revised 9 November 2008
Available online 18 November 2008

Keywords:
^{1}H NMR
Longitudinal relaxations T_1
Transverse relaxation T_2
Laplace inversion
T_1–T_2 correlation maps
Strongly inhomogeneous magnetic fields
One-sided mobile NMR
NMR-MOUSE
Cross-linked natural rubber

ABSTRACT

The single-sided NMR-MOUSE sensor that operates in highly inhomogeneous magnetic fields is used to record a CPMG ^{1}H transverse relaxation decay by CPMG echo trains for a series of cross-linked natural rubber samples. Effective transverse relaxation rates $1/T_{2,\mathrm{short}}$ and $1/T_{2,\mathrm{long}}$ were determined by a bi-exponential fit. A linear dependence of transverse relaxation rates on cross-link density is observed for medium to large values of cross-link density. As an alternative to multi-exponential fits the possibility to analyze the dynamics of soft polymer network in terms of multi-exponential decays via the inverse Laplace transformation was studied. The transient regime and the effect of the T_1/T_2 ratio in inhomogeneous static and radiofrequency magnetic fields on the CPMG decays were studied numerically using a dedicated C++ program to simulate the temporal and spatial dependence of the CPMG response. A correction factor $T_2/T_{2,\mathrm{eff}}$ is derived as a function of the T_1/T_2 ratio from numerical simulations and compared with earlier results from two different well logging devices. High-resolution T_1–T_2 correlations maps are obtained by two-dimensional Laplace inversion of CPMG detected saturation recovery curves. The T_1–T_2 experimental correlations maps were corrected for the T_1/T_2 effect using the derived $T_2/T_{2,\mathrm{eff}}$ correction factor.

1. Introduction

Nowadays, strongly inhomogeneous static and radio frequency magnetic fields become an accepted environment for the development of various NMR techniques. More and more NMR applications are being proposed and successfully operate in such fields [1]. These techniques and applications include stray-field NMR at high field [2], and surface NMR spectrometers [3,4] and sensors at low field [5–8] for material testing [8–12], biomedicine [8,13], imaging [14,15] and well logging [16–19]. Moreover, approaches toward high-resolution *ex-situ* NMR spectroscopy have been realized [20–23]. In the last years, single-sided NMR with sensors like the NMR-MOUSE presents an important advance in obtaining relevant microscopic information for the characterization of diverse types of materials [6–13]. Among these materials are elastomers with a broad range of important applications [8–12].

The CPMG sequence is widely used in NMR relaxometry to rapidly acquire NMR decays bearing information on molecular dynamics on time scale covering several orders of magnitude and that are suitable to characterize most organic liquid and soft-solid samples. The CPMG multi echo train decay in strongly inhomogeneous magnetic fields is generated by a combination of stimulated and Hahn echoes. Many important features of the CPMG pulse sequence are discussed in [9,18] and there are some techniques to optimize the pulse amplitude, phase, duration and inter-echo time. For example, the amplitudes of the first few echoes exhibit a characteristic transient behavior which quickly approaches to a smooth asymptotic behavior [18]. This effect can be neglected by skipping the first echoes or can be corrected by a function derived from numerical simulations. Relaxation in inhomogeneous fields leads to a signal decay that is in general non-exponential with an initial decay rate that is a weighted function of T_1^{-1} and T_2^{-1}. By using the CPMG pulse sequence the difference in T_1 and T_2 values leads to an error in the determinations of the transverse relaxation time, denoted in this case by $T_{2,\mathrm{eff}}$. Goelman and Prammer [17] and Hürlimann and Griffin [18] have presented numerical results for $T_{2,\mathrm{eff}}$ as a function of the ratio of T_1/T_2 for two different NMR logging devices. At long times, the echo amplitudes decay to a finite value. Hürlimann and Griffin have shown that by means of appropriate phase cycling this effect can be eliminated. Recently, the possibility to encode information directly into the shape of the CPMG echoes was demonstrated [24].

* Corresponding authors.
E-mail addresses: rfechete@phys.utcluj.ro (R. Fechete), bluemich@mc.rwth-aachen.de (B. Blümich).

1090-7807/$ - see front matter © 2008 Elsevier Inc. All rights reserved.
doi:10.1016/j.jmr.2008.11.004

This approach allows single-shot measurements of diffusion and T_1.

The analysis of CPMG echoes amplitudes is made by fitting the experimental data with two- or three-exponential functions or a stretched exponential function for the soft solid materials and by a multi-exponential function via 1D Laplace inversions for liquids imbibed in porous media [24, and references therein]. There are multiple algorithms to compute the inverse Laplace transform. In the last decade a novel algorithm for fast two-dimensional inverse Laplace transformation have been developed to obtain T_1–T_2 correlation maps [25–27]. The algorithm efficiently performs a least-squares fit on two-dimensional data sets with the constraint of non-negative amplitude. After reductions of the data set by singular value decomposition (SVD), the Tikhonov regularization method is used to balance the residual fitting errors and the known noise amplitude. The results obtained using this algorithm are stable in the presence of noise.

Two-dimensional T_1–T_2 correlation spectra were obtained using the fast 2D Laplace inversion by Song et al. [27]. The applicability of this algorithm was demonstrated by recording the 2D T_1–T_2 correlation maps at different signal-to-noise ratios for several brine-saturated rock samples. The inverse 2D Laplace transform has been applied to various scenarios like the measurement of diffusion–relaxation distribution functions D–T_2, and relaxation–relaxation distribution functions like T_1–T_2 as well as T_2–T_2 exchange. These methods can be used for fluid identification and characterization of the pore geometry in porous media based on the effects of restricted diffusion of water saturated sedimentary rock [26] and rock cores prepared in a succession of different saturation states of brine and crude oil [28]. These techniques originally developed to characterize fluid filled porous media with applications to well-logging are now also being applied to study relaxation and diffusion in static gradients for the characterization of food products [29]. 2D correlations between relaxation and/or diffusion have been used by Godefroy and Callaghan to investigate diverse liquid based samples like water and oil dynamics in food and micro-emulsions systems [30]. Washburn and Callaghan introduced a novel propagator-resolved transverse relaxation exchange type of experiment that expands the 2D Laplace technique by a dimension of spatial resolution [32]. T_2–T_2 exchange plots corresponding to different spatial displacements of the spin bearing water molecules in a porous sand matrix were obtained. Marigheto et al. [33] have developed further methods that allow peak assignment in low-resolution multidimensional NMR cross-correlation data. They demonstrate that T_1–T_2 spectra can be used as a *finger-print* to monitor the complex changes associated with phase transformations, aggregation, gelation and crystallization on a molecular scale.

Proton longitudinal and transverse relaxation times are used in homogeneous magnetic fields to describe the polymers networks dynamics directly via the mixed echoes [34,35], multipolar spin states [36,37] and indirectly by observing small solvent molecules incorporated as spies inside polymer network [38]. The aim of this paper is to discuss the polymer network dynamics mapped by ^{1}H longitudinal and transverse relaxation times in inhomogeneous magnetic fields and to test the sensitivity of different methods to different material properties for a series of cross-linked natural rubber (NR) samples. The dynamics of soft polymer network were studied in terms of multi-exponential decays and the inverse Laplace transforms. High resolution T_1–$T_{2,\mathrm{eff}}$ correlations maps are obtained for all NR samples by bi-dimensional Laplace inversion of CPMG detected saturation recovery curves. The T_1–$T_{2,\mathrm{eff}}$ correlations maps were corrected for the T_1/T_2 effect using the derived $T_2/T_{2,\mathrm{eff}}$ correction function.

2. Experimental

The preparation and microscopic to macroscopic properties correlations of investigated elastomers sample series were already reported on some previous work [8,10–12,34–38]. Proton relaxation times were measured with a BRUKER Minispec spectrometer connected to a bar magnet NMR-MOUSE® sensor with a butterfly coil working at 19.2 MHz. The sample was placed on top of the NMR sensor directly on the coil surface and 4 mm above the north pole of the permanent magnet. All measurements were performed at room temperature, i.e., at 20 ± 0.5 °C. The NR samples are denoted as NR1–NR7 according to the amount in phr of cross-linker/accelerator which scales with the cross-link density.

The ^{1}H transverse relaxation decays were measured using the CPMG (Carr–Purcell–Meiboom–Gill) pulse sequence (Fig. 1a). The excitation and the refocusing pulse durations were both set at 5.5 μs and the pulse amplitude is optimized to yield the maximum of Hahn echo amplitude. In the presence of inhomogeneities of static magnetic field the pulses became more selective with the increasing of the pulses length. Pulse amplitude modulation of the flip angle was chosen to assure the same excitation bandwidth for both pulses in view of better signal-to-noise ratio. Moreover, in order to ensure the best overlap of the Hahn and stimulated echoes and to account for resonance offset characteristic for CPMG pulse sequences in inhomogeneous magnetic fields, the duration $\tau + \tau'$ between two adjacent refocusing pulses was optimized, where τ is the duration between the excitation pulse and first refocusing pulse. The time interval, τ' between the maximum of the echo and the subsequent refocusing pulse is smaller than τ. Usually, the difference between these two durations is a fraction of the pulse duration. In our case τ = 34.5 μs and τ' = 30.0 μs was giving an interecho time of 70 μs. We have recorded 800 echoes with 1024 scans to increase the signal-to-noise ratio. The recycle delay was set to 1 s, which is a value much larger than 5 times T_1, but was chosen in order to avoid overheating the sample exposed to many long CPMG scans. The detection windows were open for 15 μs per echo with the maximum of the echo approximately in the middle of windows. We have recorded 10 points per echo in magnitude mode and the corresponding value was computed as an average of five points two before and two after the maximum of the echo.

The ^{1}H T_1–T_2 correlation data were recorded using a saturation recovery pulse sequence for longitudinal relaxation encoding, followed by a detection via a CPMG sequence for transverse relaxation encoding [27] (Fig. 1b). The parameters for the CPMG detection are similar to the ones discussed above. In this case we have used a number of 600 echoes, 512 scans with a recycle delay of 0.4 s and an interecho time of 100 μs. The longitudinal relaxation was encoded by the saturation recovery pulse sequence. The saturation of the magnetization was achieved by a series of excitation pulses with variable time intervals between them. In our case we have successively halved the time lag between 10 pulses. The recovery time, was increased in steps of 2 ms up to 200 ms to obtain 100 experiments in the indirect dimension of the 2D correlation experiments.

3. NMR measurements, simulations and data processing

3.1. ^{1}H transverse relaxation time measurements

The normalized CPMG decays for the series cross-linked natural rubber samples becomes steeper with increasing cross-link density indicating a decrease of T_2 associated with more restricted polymer chain dynamics. In a semi quantitative fashion, the CPMG decays are analyzed in terms of a bi-exponential fit:

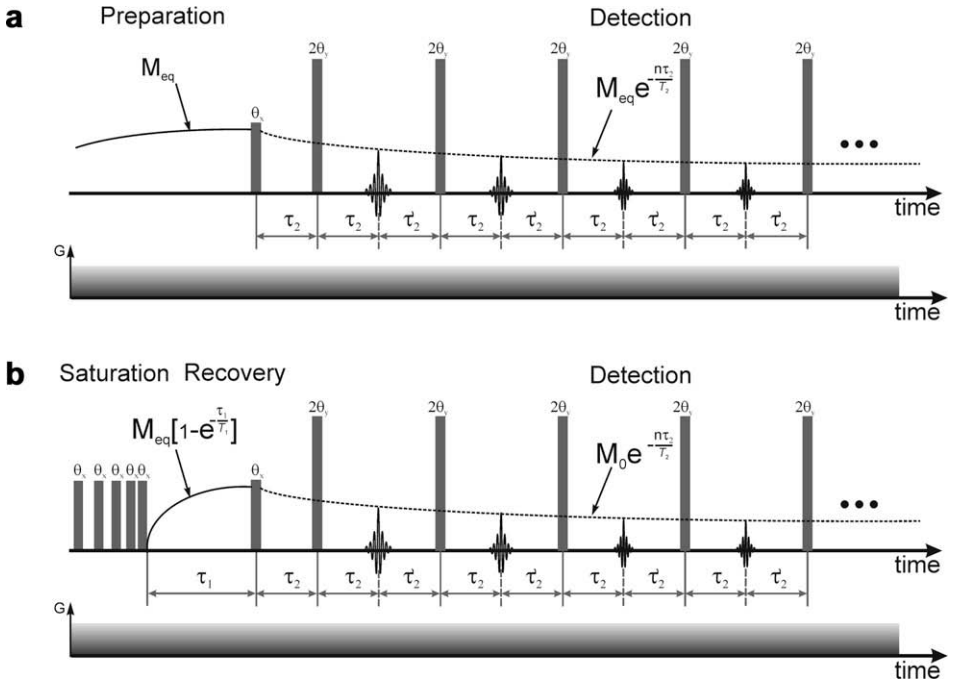

Fig. 1. The classical CPMG pulse sequence (a) and the combination of saturation recovery followed by detection via CPMG pulse sequence for recording T_1–T_2 correlations maps (b).

$$M(2n\tau) = A_{\text{short}} \exp\left\{-\frac{2n\tau}{T_{2,\text{short}}}\right\} + A_{\text{long}} \exp\left\{-\frac{2n\tau}{T_{2,\text{long}}}\right\} + A_{\text{noise}}, \tag{1}$$

where n is the number of echoes and $T_{2,\text{short}}$ and $T_{2,\text{long}}$ are the solid-like and liquid-like effective transverse relaxation times, respectively. All decays can be fit by a bi-exponential function. The dependences of the relaxation rates $1/T_{2,\text{long}}$ and $1/T_{2,\text{short}}$ on the cross-link density are shown in Fig. 2a for the liquid-like (long) component and in Fig. 2b for the solid-like (short) component of transverse decay. For medium and large values of the cross-link density **C** the dependence is found to be linear. Exception are NR1 for the long component and NR1 and NR2 for short component.

3.2. Multi-exponential analysis of CPMG data

In the last years various inverse Laplace transforms algorithms were developed [25–27,31,39], that are regularized to cope with the ill condition in the presence of noise. So far the inverse Laplace transform has been applied in NMR mostly for systems of isolated spins, like fluids in porous media [25–29] or food samples [29] and molecules undergoing diffusion [26,28–31]. The Laplace transform of the magnetization decay can be written in integral form as a function of stroboscopic time $2n\tau$ at which the CPMG echoes are observed:

$$M(2n\tau) = \int_0^\infty A(T_2) \exp\left\{-\frac{2n\tau}{T_2}\right\} dT_2 + A_{\text{noise}}(2n\tau), \tag{2}$$

where $A(T_2)$ is the probability density function to observe a given T_2 component in the transverse magnetization decay, and $A_{\text{noise}}(2n\tau)$ is the random noise at the maxima of the CPMG echoes. In practice, Eq. (2) is replaced by a sum over a finite number N of components, usually not larger than 1000:

$$M(2n\tau) = \sum_{i=1}^{N} A(T_{2,i}) \exp\left\{-\frac{2n\tau}{T_{2,i}}\right\} + A_{\text{noise}}. \tag{3}$$

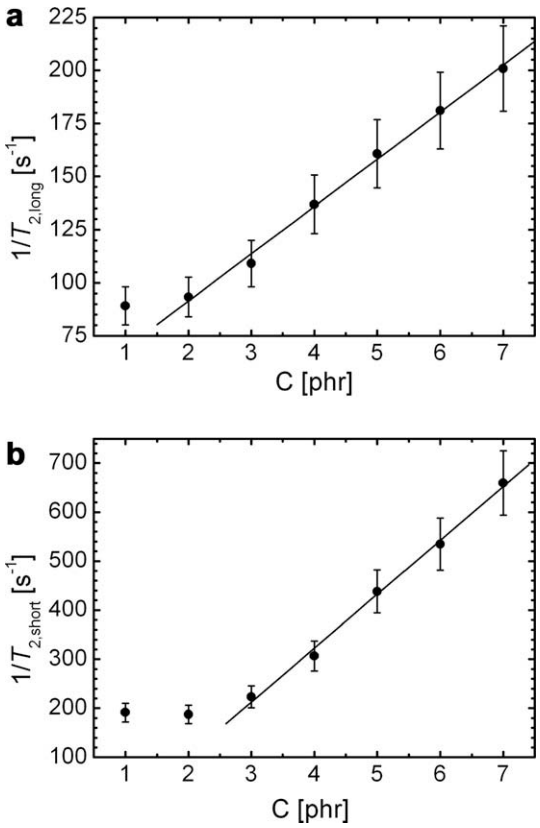

Fig. 2. Dependence of the inverse of the long (a) and short (b) transversal relaxation times as a function of cross-link density, C. With the exception of low cross-link density, the dependence is linear.

In order to obtain $A(T_{2,i})$, a fast inversion algorithm was used [25–27], based on singular value decomposition of associated matrices, a transformation into a reduced problem and a regularization algorithm. The regularization procedure is controlled by the

regularization parameter α, which depends on the signal-to-noise ratio and impacts the final result [27]. There are algorithms and rules to choose the best value of α but to compare the results and based on a very good signal to noise ratio we have chosen $\alpha = 1$.

The CPMG echo decays of the natural rubber samples NR1–NR7 were analyzed by the Laplace Inversion assuming that they can be described by a multi-exponential function (Fig. 3). For a good definition of the peaks we have used 500 points on the logarithmic scale of T_2 values. The data of sample NR1 with the lowest cross-link density are shown in the back of the figure. A single line with pronounced left shoulder is observed. This shoulder at small T_2 values can be an indication of a bimodal polymer chain dynamic even at small values of the cross-link density. Due to the large line width, both lines overlap and a single asymmetric line is observed. In terms of an analysis by fits with a bi-exponential function such an overlap can lead to errors in the extracted values of transverse relaxation times. By applying the Laplace inversion to the CPMG decays the polymer dynamic appear to be revealed better than by a simple bi-exponential analysis. The integrals over the peaks are proportional to number of spins characterized by similar dynamic behavior. The widths of the peaks inform about the heterogeneities of a particular behavior.

The T_2 distributions can arise from the properties of the studied samples but also as a result of the particular NMR experiment. It is well known [18] that in inhomogeneous magnetic fields the CPMG decay is determined not only by the transverse relaxation time but it is also affected by the T_1/T_2 ratio. Consequently, a simple analysis of CPMG data by Laplace inversion can be subjected to systematic errors. The resultant 1D distributions of T_2 values can be a superposition of multiple distributions characterized by different T_1 values. Moreover, a particular value of the T_1/T_2 ratio can result in a shift of the observed T_2 value resulting in the value $T_{2,\mathrm{eff}}$ of the effective transverse relaxation time.

In the following the effect of the T_1/T_2 ratio on the values of $T_{2,\mathrm{eff}}$ measured by the NMR-MOUSE®, a sensor with highly inhomogeneous static and radiofrequency magnetic fields, is estimated. The approach to estimate the effect of the T_1/T_2 ratio on the measured CPMG decay in a strongly inhomogeneous magnetic field is to simulate the NMR response of a standard sample measured with the NMR-MOUSE® sensor. CPMG decays are simulated as a function of T_1/T_2 ratio for a sample described by well-known values of longitudinal and transverse relaxation times, and the $T_{2,\mathrm{eff}}$ value is extracted.

3.3. Numerical characterization of the NMR-MOUSE®

For unilateral NMR sensors with strong field gradients, the NMR signal is determined by the spin system response in homogeneous field to a specific pulse sequence and the particular characteristics of NMR device, in particular the static and radiofrequency magnetic field inhomogeneities. In order to characterize and quantify the influence of the NMR sensor characteristics on the NMR observables, a numerical simulation of the spin-system response is essential. The NMR sensor can be described in full by the spatial distribution of the static and radiofrequency magnetic fields and the filter functions. Two numerical simulation programs, written in C++ were used to generate the static and radiofrequency magnetic field maps. These maps were used together with the pulse sequences as input information for another C++ program to calculate the spin system response in the given inhomogeneous magnetic fields.

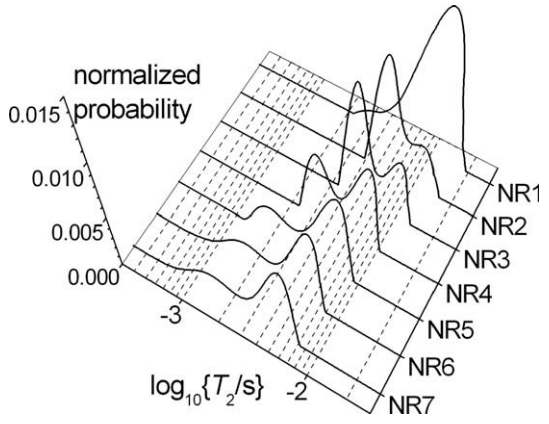

Fig. 3. Distributions of transverse relaxation times T_2 obtained from Laplace inversions of the CPMG echoes trains for the rubber samples NR1–NR7.

The first step in our approach is the generation of static magnetic field $\vec{B}_0(\vec{r})$ map. Due to the large inhomogeneities, the sample is divided into small volume elements, hereafter called voxels, in which the magnetic fields can be considered constant. The magnetic fields are computed in each of this volume element to generate numerical maps. The static magnetic field produced by the permanent magnet has been considered to be a Coulombian field by using the surface charge approximation [9,40]. Considering an arbitrary, but unique reference frame, the static magnetic field at a point $\vec{r}$ was computed by considering magnetic charges distributed on the pole surfaces of the permanent magnets:

$$\vec{B}_0(\vec{r}) = k\left[\int_{S_N} \frac{\vec{r}-\vec{r}_N}{|\vec{r}-\vec{r}_N|^3}\,ds - \int_{S_S} \frac{\vec{r}-\vec{r}_S}{|\vec{r}-\vec{r}_S|^3}\,ds\right], \tag{4}$$

where S_N and S_S are the North and South pole surfaces, and $\vec{r}_N$ and $\vec{r}_S$ denote the position of the surface elements. The symbol $|(\cdots)|$ denote the vector modulus. The mesh size of the integration grid was 0.1 mm, and the constant k was determined by fitting the computed values to the measured ones for the particular NMR-MOUSE® used.

Modulus $|\vec{B}_0|$ maps of the static magnetic field for planes parallel to the North pole surface of the magnet are presented in Fig. 4 as function of distance z from the magnet surface. The distance is measured from the top of the radiofrequency coil, which is at 4 mm above the pole surface. The magnetic field maps are centered in the magnet center and extended in x and y direction to cover the main influence of a square 20×20 mm radiofrequency coil. The slice $z = 0$ mm (Fig. 4a) corresponds to a plane directly on top of the radiofrequency coil and to the maximum of the Larmor frequency. The working frequency was set to be 19.2 MHz which correspond to a sensitive volume centered approximately at $z = 0.2$ mm (Fig. 4b). The position $z = 0.5$ mm marks a transition regime in the $|\vec{B}_0|$ maps (Fig. 4c) to the particular value $z = 1$ mm above the radiofrequency coil, where the modulus of the static magnetic field distribution is the least inhomogeneous (Fig. 4d).

For a better view of the magnetic field inhomogeneity, four contour lines cover the middle areas of the field maps where the region of interest is located. All four maps are drawn to the same scale for better comparison of the field distributions in the plane and their depth dependence. An general observation is the asymmetry of the $|\vec{B}_0|$ maps in x and y directions This is due to the fact that the magnet cross section (45×40 mm) is not a square. The magnetic field is more curved along the x direction than in the y direction. Associated with the large gradients of 10–36 T/m of this type of magnet [8] along the z direction is a relatively well defined localization of the NMR signal. A large homogeneous area can be observed centered in the middle of the field maps. For planes parallel to the pole surface, the magnetic field distributions differ according to the distance from the surface. Close to the magnet pole, the magnetic field decreases from edges to the middle (Fig. 4a and b) and far away from the surface, the magnetic field is higher in the middle position than at the edges. The transition

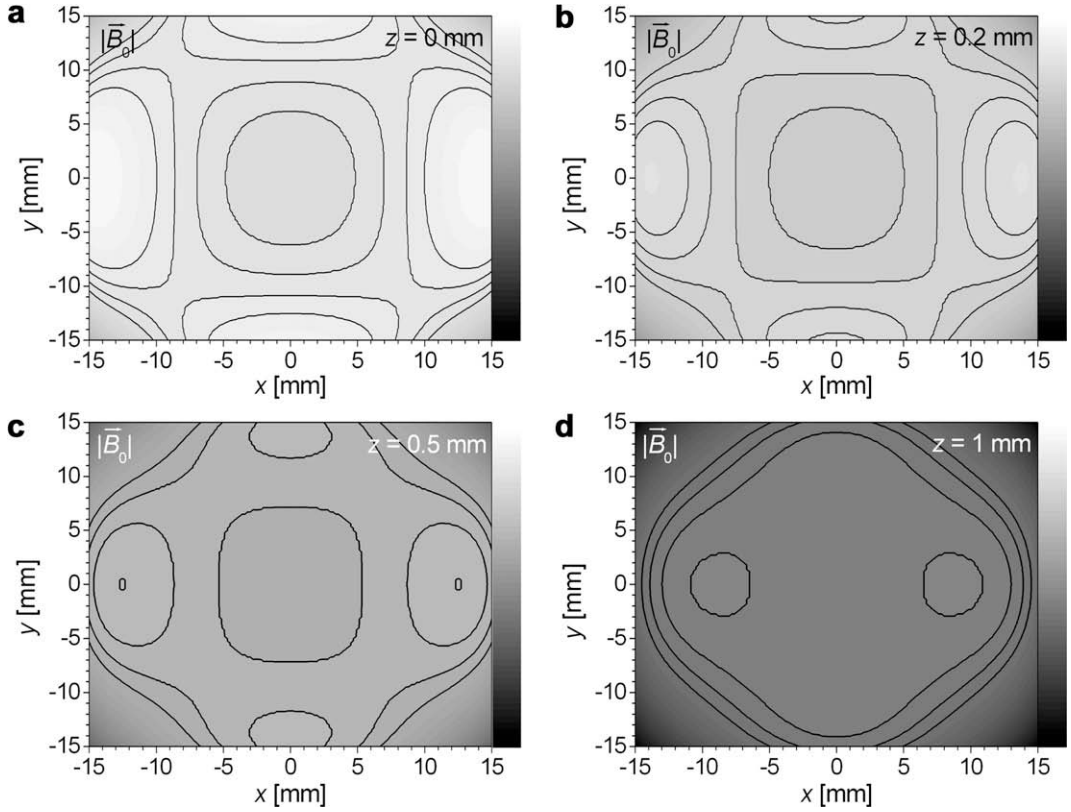

Fig. 4. Spatial distributions of the modulus of the static magnetic field in the *xy* plane of a 40 × 45 × 50 mm bar magnet for different values of *z*. (a) *z* = 0 mm; (b) *z* = 0.2 mm; (c) *z* = 0.5 mm; (d) *z* = 1.0 mm.

from one extreme to the other is not sudden, and a homogeneous distribution of the modulus of the static magnetic field must occur in a given intermediate plane (Fig. 4d). There the sensitive volume extended over a large area, which is also influenced by the shape and dimension of the radiofrequency coil.

The map of the radiofrequency magnetic field $\vec{B}_1(\vec{r})$ produced by the transmitter coil was calculated according to the Biot-Savart law:

$$\vec{B}_1(\vec{r}) = \frac{\mu_0 I}{4\pi} \oint_\Gamma \frac{(\vec{r}_c - \vec{r}) \times d\vec{r}_c}{|\vec{r}_c - \vec{r}|^3} = I \cdot \vec{b}_{RF}(\vec{r}), \quad (5)$$

where I is the intensity of the electrical current in the radiofrequency coil, μ_0 is the vacuum permeability, $\vec{r}_C$ is the position of the current element of length $d\vec{r}_C$ which moves along the curve Γ that describes the windings of the coil. A unique magnetic flux density map $\vec{b}_{RF}(\vec{r})$ is computed for a unitary current so that the pulse amplitude can be set simply by a particular value to the current I. The same radiofrequency map is used to compute the electrical signal induced in the receiver coil by the time-dependent magnetization as the transmitter and receiver coils coincide.

Maps of the modulus of the radiofrequency magnetic field generated for a current of 1 A are presented in Fig. 5 in the same planes as for the static magnetic field parallel to pole surface of the magnet as a function of distance to this pole surface. The z distance is measured from the top surface of the radiofrequency coil. All maps are drawn to the same scale with the maximum corresponding to the maximum value of the radiofrequency field at z = 0 mm corresponding to the top of the transmitter/receiver coil (Fig. 5a), and the minimum corresponding to the minimum value in the map for z = 1 mm (Fig. 5d).

The $|\vec{B}_1|$ map of Fig. 5a is a good image of the coil as it maps the $|\vec{B}_1|$ distribution directly on top of the wire where the radiofrequency field is highest. The coil was etched on a two sided copper plated PC board with mirror images on both sides. In the center gap of the conductors a thermocouple was mounted to sense the temperature. The particular coil used was a butterfly coil constructed from two figure-8 coils [5]. A figure-8 coil produces a magnetic field that emanates from one current loop closing the path from the opposite side. The radiofrequency magnetic field capable of inducing an electrical current in the figure-8 coil must have the same near field symmetry. Contrary, external noise originate from far field and the associated electromagnetic waves pass through both loops of the figure-8 coil from the same side, inducing in the coil two currents with opposite signs that cancel each other.

The amplitude of the radiofrequency magnetic field decay decrease with increasing distance from the coil surface, effect observed in Fig. 5 by the brightness of the $|\vec{B}_1|$ maps. With increasing distance from the coil, the coil shape become less and less visible is indicating a decrease of the lateral B_1 and an increase in homogeneity of the radiofrequency field. The $|\vec{B}_1|$ map given at z = 1 mm (Fig. 5d) presents only the general features of the transmitter/receiver coil while the particular features vanish. At first sight and noting also the static magnetic field map at z = 1 mm, one can conclude that at this distance NMR experiments are performed in more homogeneous magnetic fields. Unfortunately, this is not entirely true, as one should bear in mind that only the field magnitude are shown. In Fig. 4 is missing information on the relative orientation of the $\vec{B}_0$ and $\vec{B}_1$ fields, so that the homogeneity of the sensitive volume is lower.

3.4. Radio-frequency pulse sequence and spin response

As a first approximation an isolated ½ spin system is considered interacting with two magnetic fields $\vec{B}_0(\vec{r})$ and $\vec{B}_1(\vec{r})$. In inhomogeneous magnetic fields the majority of voxels described by the position vector $\vec{r}$ is out of resonance. The local precession frequency $\omega_0(\vec{r}) = -\gamma B_0(\vec{r})$ relates to the external static magnetic field and

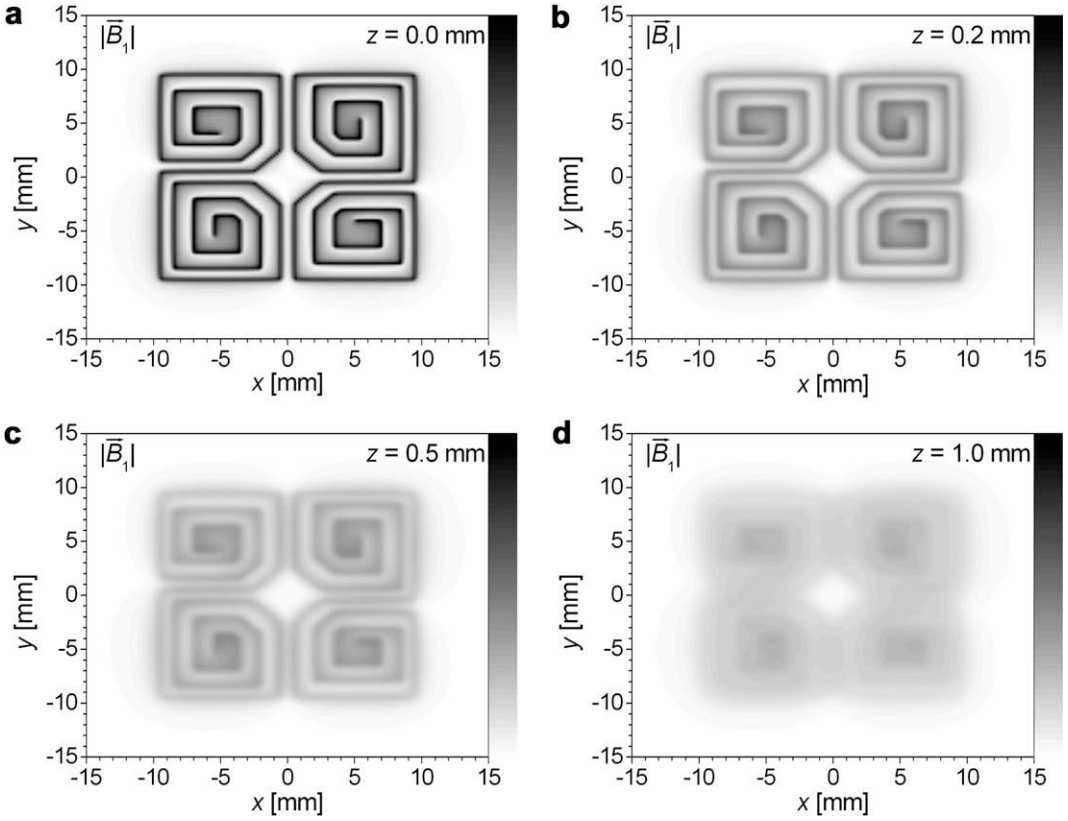

Fig. 5. Spatial distributions of the modulus of the radiofrequency magnetic field in the *xy* plane of a butterfly coil for different values of *z*. (a) *z* = 0 mm; (b) *z* = 0.2 mm; (c) *z* = 0.5 mm; (d) *z* = 1.0 mm.

the magnetogyric ratio by the Larmor theorem. In the rotating frame resonance offset is defined as:

$$\Delta\omega(\vec{r}) = \omega_{\mathrm{TR}} + \omega_0(\vec{r}) = \omega_{\mathrm{TR}} - \gamma B_0(\vec{r}). \tag{6}$$

The linearly polarized radiofrequency magnetic field density $\vec{b}_{\mathrm{RF}}(\vec{r})$ is understood to arise from two circular polarized fields of which only one leads to transitions. It is therefore replaced by 2 $\vec{B}_1(\vec{r})$. Moreover, in inhomogeneous magnetic fields, one needs to consider the component of $\vec{B}_1(\vec{r})$ orthogonal to $\vec{B}_0(\vec{r})$ (henceforth denoted by $\vec{B}_{1,n}(\vec{r})$) as the one that induces transition because the parallel component commutes with the Zeeman Hamiltonian. Similar to the Larmor frequency in static magnetic field, the nutation frequency is defined by the normal component of the radiofrequency magnetic field $\omega_1(\vec{r}) = -\gamma B_{1,\mathrm{n}}(\vec{r})$. In the presence of both fields the precession takes places around the effective field with the effective precession frequency:

$$\omega_{\mathrm{eff}}(\vec{r}) = \sqrt{\Delta\omega^2(\vec{r}) + \omega_1^2(\vec{r})}. \tag{7}$$

For isolated spins the evolution during pulses and free precession periods can simply be described by rotations of spin components around *x*, *y* and *z* axes. A rotation around the *z*-axis by an angle θ is expressed by the rotation matrix:

$$\mathbf{R}_z(\theta) = \begin{pmatrix} \cos\theta & -\sin\theta & 0 \\ \sin\theta & \cos\theta & 0 \\ 0 & 0 & 1 \end{pmatrix}. \tag{8}$$

The other rotation matrices are:

$$\mathbf{R}_x(\theta) = \begin{pmatrix} 1 & 0 & 0 \\ 0 & \cos\theta & -\sin\theta \\ 0 & \sin\theta & \cos\theta \end{pmatrix}, \quad \mathbf{R}_y(\theta) = \begin{pmatrix} \cos\theta & 0 & \sin\theta \\ 0 & 1 & 0 \\ -\sin\theta & 0 & \cos\theta \end{pmatrix}. \tag{9}$$

In inhomogeneous magnetic fields the rotation matrix of a general pulse of duration, *t* and transmitter phase ϕ_{TR} can be expressed as a combination of five rotations matrices:

$$\mathbf{P}(\vec{r}, t, \varphi_{\mathrm{TR}}) = \mathbf{R}_z(-\varphi_{\mathrm{TR}})\mathbf{R}_y(-\theta(\vec{r}))\mathbf{R}_z(\omega_{eff}(\vec{r})t)\mathbf{R}_y(\theta(\vec{r}))\mathbf{R}_z(\varphi_{\mathrm{TR}}), \tag{10}$$

where $\theta(\vec{r}) = \arccos\left(\frac{\Delta\omega(\vec{r})}{\omega_{\mathrm{eff}}(\vec{r})}\right)$.

The pulse phase is the same in every voxel. But depending on $\omega_{\mathrm{eff}}(\vec{r})$ the effect of the pulse is different from voxel to voxel as the static and radiofrequency magnetic fields vary. A general expression of the density operator at every moment in time can be written as:

$$\rho(\vec{r}, t) = C_x(\vec{r}, t)\hat{I}_x + C_y(\vec{r}, t)\hat{I}_y + C_z(\vec{r}, t)\hat{I}_z, \tag{11}$$

where $C_x(\vec{r}, t)$, $C_y(\vec{r}, t)$ and $C_z(\vec{r}, t)$ are three space-time-dependent variables that describe the *x*, *y* and *z* components of the magnetization. Then the density operator after a pulse is given by:

$$\rho(\vec{r}, \tau + t) = \hat{\mathrm{P}}(\vec{r}, t, \varphi_{\mathrm{TR}})\rho(\vec{r}, \tau). \tag{12}$$

For isolated spins the free evolution is a rotation around the *z*-axis, i.e.:

$$\mathbf{E}(\Delta\omega t) = \mathbf{R}_z(\Delta\omega t). \tag{13}$$

Relaxation is implemented following the Bloch equations:

$$C_{x,y}(\vec{r}, \tau + t) = C_{x,y}(\vec{r}, \tau)e^{-\frac{t}{T_2}}, \tag{14}$$

$$C_z(\vec{r}, \tau + t) \quad = C_z(\vec{r}, \tau)e^{-\frac{t}{T_1}} + C_\infty(1 - e^{-\frac{t}{T_1}}). \tag{15}$$

The variables $C_i(\vec{r}, \tau)$, $i = x, y, z$ (Eq. (10)) contain information related to the previous evolution of spin system, and the C_∞ is related to the normalized equilibrium magnetization.

3.5. The theorem of reciprocity and the NMR signal

The electrical signal induced in the receiver coil by a magnetic moment $\vec{m}(\vec{r},t)$ of a volume element of the sample at position $\vec{r}$ is given by the theorem of reciprocity, taking into account the electromagnetic induction laws [9]:

$$e = -\frac{\partial \Phi_m}{\partial t} = -\frac{\partial}{\partial t}\left[\int_S (\vec{B}_m \vec{n}) dS\right] = -\frac{\partial\left[\vec{m}(t)\vec{b}_{RF}(\vec{r})\right]}{\partial t} = -\frac{\partial \vec{m}(t)}{\partial t}\vec{b}_{RF}(\vec{r}), \tag{16}$$

where Φ_m is the magnetic flux through the coil created by the magnetic moment

$$\vec{m}(t) = \gamma\hbar \cdot \mathrm{Tr}\{\vec{I}\cdot\rho(t)\}, \tag{17}$$

and the $\vec{B}_m$ is the corresponding flux density, and $\vec{n}$ is the unit vector of the infinitesimal element dS orthogonal to the coil surface. The reciprocity theorem is related to the fact that the electromotive voltage induced by a magnetic moment $\vec{m}(\vec{r},t)$ at position $\vec{r}$ in the coil, is proportional to the magnetic field density, $\vec{b}(\vec{r})$ produced by the coil at the position of the magnetic moment.

Two important factors that must be considered for realistic simulations of the NMR response in inhomogeneous magnetic fields are the sensor and receiver filters. The complex sensor filter is implemented as a product:

$$f(\omega_0(\vec{r}),\omega_{RX},Q) = f_A(\omega_0(\vec{r}),\omega_{RX},Q)\exp\{-i f_\varphi(\omega_0(\vec{r}),\omega_{RX},Q)\}, \tag{18}$$

of an amplitude function:

$$f_A(\omega_0(\vec{r}),\omega_{RX},Q) = \frac{1}{\sqrt{1+Q\left(\frac{\omega_0(\vec{r})}{\omega_{RX}}-\frac{\omega_{RX}}{\omega_0(\vec{r})}\right)^2}}, \tag{19}$$

and a phase function:

$$F_\varphi(\omega_0(\vec{r}),\omega_{RX},Q) = \arctan\left[Q\left(\frac{\omega_0(\vec{r})}{\omega_{RX}}-\frac{\omega_{RX}}{\omega_0(\vec{r})}\right)\right]. \tag{20}$$

The quality factor of the coil circuit is denoted by Q, and receiver frequency by ω_{RX}. The spectrometer receiver will impose a supplementary amplitude modulation, seen as a filter with receiver bandwidth, f_c of the signal at the Larmor frequency, $\omega_0(\vec{r})$:

$$S_{rec}(\omega_0(\vec{r}),\omega_{RX},f_c) = \frac{1}{\sqrt{1+\left(\frac{\omega_0(\vec{r})-\omega_{RX}}{2\pi f_c}\right)^8}} + 0i. \tag{21}$$

The large value of the exponent ensures a band-pass like shape of the filter.

The real and imaginary parts of the time domain signal are given by:

$$\begin{aligned} S_x(t) &= \int_V S_x(\vec{r},t)dV \\ S_y(t) &= \int_V S_y(\vec{r},t)dV \end{aligned}, \tag{22}$$

where the integral is considered over the entire sample volume V of the real (x) and imaginary (y) signal component in each voxel:

$$\begin{aligned} S_x(\vec{r},t) &= \mathscr{K}(\vec{r},t)\, f_A(\omega_0(\vec{r}),\omega_{RX},Q)\, S_{rec}(\omega_0(\vec{r}),\omega_{RX},f_c) \\ &\quad\times\cos[\Delta\omega t+\alpha(\vec{r})-\delta+f_\varphi] \\ S_y(\vec{r},t) &= \mathscr{K}(\vec{r},t)\, f_A(\omega_0(\vec{r}),\omega_{RX},Q)\, S_{rec}(\omega_0(\vec{r}),\omega_{RX},f_c) \\ &\quad\times\sin[\Delta\omega t+\alpha(\vec{r})-\delta+f_\varphi] \end{aligned}, \tag{23}$$

with $\alpha(\vec{r}) = \arctan\left(-\frac{C_x(\vec{r})}{C_y(\vec{r})}\right)$ and the receiver phase, δ.

The last point is to scale the value by the constant K that multiplies the local signals from Eq. (22) so the simulated NMR signal can be expressed in μV and not into arbitrary units. The origin of this value is related to the equilibrium magnetization, or the total magnetization per volume unit:

$$\mathscr{M}_0 = \mathscr{N}\frac{\gamma^2\hbar^2 B_0 I(I+1)}{3k_B T}, \tag{24}$$

with $\mathscr{N}$ the number of spins per volume unit, γ the gyromagnetic ratio, I the nuclear spin quantum number, $\hbar$ reduced Planck constant, k_B the Boltzmann constant and T the absolute temperature. We have to consider the static magnetic field in each voxel dependent on position as well as the voxel value of the radiofrequency magnetic field. Due to the time derivative (Eq. (15)) of the magnetic moment, the Larmor frequency or its negative and the product between the gyromagnetic ratio and static magnetic field must be also considered. The spin evolution is described by the transverse magnetization or the time-dependent x and y components of magnetizations, C_x and C_y. Taken all together, the voxel dependent multiplication constant is obtained as:

$$K(\vec{r},t) = -\mathscr{N}\frac{\gamma^3\hbar^2\Delta V}{4k_B T}B_0^2(\vec{r})b_{1,n}(\vec{r})\sqrt{C_x^2(\vec{r},t)+C_y^2(\vec{r},t)}. \tag{25}$$

3.6. Magnetic field inhomogeneity and slice selection

A map of the magnetic field modulus, $|\vec{B}_0|$ for the bar magnet NMR-MOUSE® in a vertical xz plane through the origin at $y = 0$ is shown in Fig. 6a. The x direction ranges from −15 mm to +15mm, large enough to cover the radiofrequency coil. The position $z = 0$ mm corresponds to the upper surface of the radiofrequency coil which is at 4 mm above the north pole of the permanent magnet. The z scale is stretched to reveal some useful features. Close to the surface of the permanent magnet, the magnetic field is largest near the magnet edges. With increasing distance z from the surface, the magnetic field becomes more homogeneous along the x direction. For example, near $z = 1$ mm we can observe an isosurface in a horizontal plane, as outlined by the black lines in the middle. From an NMR point of view, this plane can be used to select a planar slice through the sample at the given depth.

The static magnetic field imposes limitation on the sensitive volume. Further limitation is imposed also by the radiofrequency magnetic field (Fig. 6b). The $|\vec{B}_1|$ map produced by the unitary current through the butterfly coil in the same xz plane centered at $y = 0$ is far more inhomogeneous than that of the static magnetic field generated in the same region. The inhomogeneities are largest close to the copper conductors of the coil at low values of z close to $x = \pm 10$ mm. Contrary to the $|\vec{B}_0|$ isosurface lines which extended in the x direction, the $|\vec{B}_1|$ isosurface lines cover relatively short distances in both x and z directions.

A C++ program was written to compute the spin response following the concepts presented above using as input the static and radiofrequency magnetic field maps of the NMR sensor, the pulse sequence of the particular experiment and the T_1 and T_2 values of the sample. The sensitive volume or the spatial distribution of the spin response calculated as the magnitude of the real and imaginary magnetization components following an excitation pulse for different transmitter/receiver frequencies of 16.5, 17.5, 18.5 and 19.2 MHz, the valued used in our conditions, are presented in Fig. 7. The duration of excitation pulse was 5.5 μs, and the relaxation times of $T_1 = 1$ s and $T_2 = 1$ s, practically have no influence on tens of microseconds scale. The most important factors that influence the sensitive volume are the NMR sensor and receiver parameters, because these affect the filter properties as described in Eqs. (17)–(20). The quality factor was set to be $Q = 20$ and the receiver bandwidth $f_c = 5$ kHz. The gap in the sensitivity volume around $x = 0$ mm is due to the fact that near this

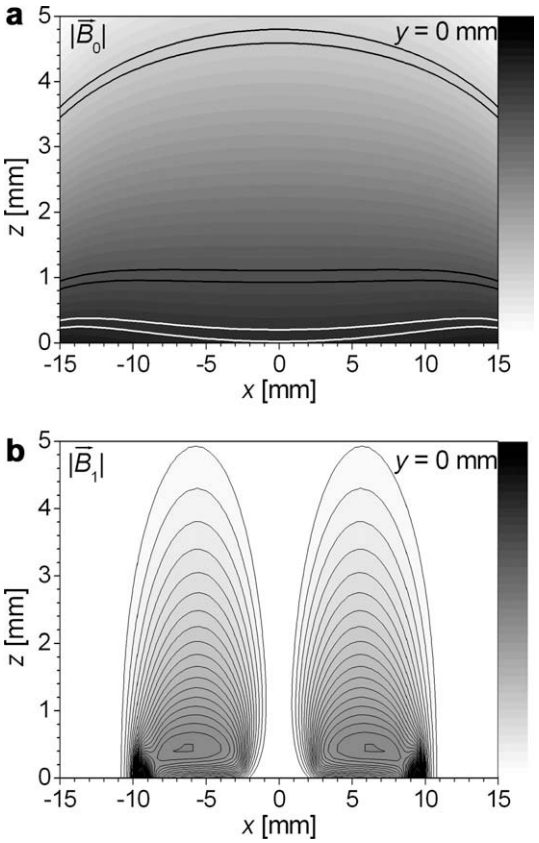

Fig. 6. Magnetic field maps of the modulus of static, (a) and radiofrequency, (b) magnetic fields in the vertical plane as a function of x and z coordinates for $y = 0$ mm. This characterizes the bar magnet NMR-MOUSE® with a butterfly coil. The position $z = 0$ mm in the magnetic field maps corresponds to a distance of 4 mm above the north pole of the magnet and a 0.1 mm above the surface of butterfly coil.

position the radiofrequency magnetic field has a very low value as in Fig. 6b. With decreasing transmitter/receiver frequency slices at different sample depth can be selected.

Contrary to NMR in homogeneous magnetic fields, where the sensitive volume is contiguous, in inhomogeneous magnetic fields the sensitive volume may depend on the value and orientation of $\vec{B}_1$ with respect to $\vec{B}_0$, and also on the particular pulse sequence. This aspect is discussed in the next section.

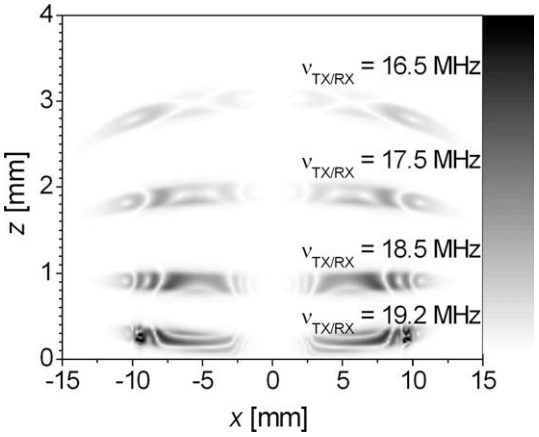

Fig. 7. Simulation of the spatial variations of the sensitive volume of a bar magnet NMR-MOUSE® with a butterfly coil. For different transmitter/receiver frequencies $\nu_{TX/RX}$ = 19.2 MHz, $\nu_{TX/RX}$ = 18.5 MHz, $\nu_{TX/RX}$ = 17.5 MHz, and $\nu_{TX/RX}$ = 16.5 MHz the resonant regions are identified in the vertical xz plane at $y = 0$ mm.

3.7. Sensitive volume of the bar-magnet NMR-MOUSE with a butterfly coil for the CPMG pulse sequence

The sensitive volume is determined not only by the features of the NMR sensor, but its shape in space can also change with time after each pulse. Fig. 8 depict the sensitive volume in a horizontal plane at $z = 0.2$ mm above the radiofrequency coil after the first pulse and for maximum value of the first, second, fifth, tenth and hundredth echo for a CPMG pulse sequence in terms of the maximum NMR signal. The Larmor frequency of 19.2 MHz and pulse sequence parameters were set those of the measurements presented below with the exception of the spin-spin relaxation time which was set to 10 s so that simulation time scale can be considered to be infinite and without any influence on the sensitive volume. Due to the magnet asymmetry, the sensitive volume is not symmetric in horizontal xy plane. For better comparison of the sensitive volumes at different moments in time during the CPMG sequence figures are all drawn to the same scale.

Fig. 8a shows the simulated sensitive volume after the first pulse. It is an accurate representation of the radiofrequency coil. The continuous lines of high intensity follow the coil pattern, decreasing gradually in the middle, as the magnetization becomes off resonance. The intensity decreases also fast with the increasing distance from the coil conductor in the horizontal plane, leading to a good map of the coil shape. However, the first refocusing pulse induces dramatic changes in the sensitive volume of the first echo (Fig. 8b). The general features remain similar to those in Fig. 8a but the sensitive volume becomes fractionated and signal is acquired from the space between the conductors. This is followed with the sensitive volume for the echo number two (Fig. 8c). A coherent pattern of stripes that follows the isolines of the static magnetic field is barely observable in the middle. The subsequent radiofrequency pulses scramble the features in the sensitive volume more and more leading to an increased volume compared to that of Fig. 8a. Moreover, after an initial transitory regime, a steady state regime is reached in the evolution of the sensitive volume at high echo numbers (Fig. 8d–f).

3.8. Numerical characterization of T_1 and T_2 mixing effects in CPMG measurements

In the inhomogeneous magnetic field the on-resonance condition is fulfilled only for a very small number of voxels. The majority of voxels from the sensitive volume is out of resonance, and therefore, is not possible to achieve a perfect $\pi/2$ pulse. A direct consequence is the fact that at every moment during the CPMG pulse sequence, the total nuclear magnetization will be described by non-zero values of all three components along the x, y and z directions. An exception is the first echo, which is a pure Hahn echo. The others are mixed, inhomogeneous echoes, i.e., superpositions of Hahn echoes, characterized only by evolution in the transverse plane and decaying with T_2, and stimulated echoes, characterized by storage of magnetization along the z direction with magnetization build-up by T_1 relaxation. As a consequence CPMG decay is weighted by transverse as well as by the longitudinal relaxation. The relative contributions of these relaxation processes in the measured signals are functions of the sensor properties i.e., the spatial distributions of static and radiofrequency magnetic fields, as well as a function of the pulse sequence parameters, like the echo time, duration and amplitude of the excitation and refocusing pulses. Moreover, the number of coherence pathways is increasing dramatically with the echo number in a CPMG pulse sequence. Therefore, without the help of computer simulations it is not possible to estimate the effect from the difference between T_2 and T_1 on the CPMG decay.

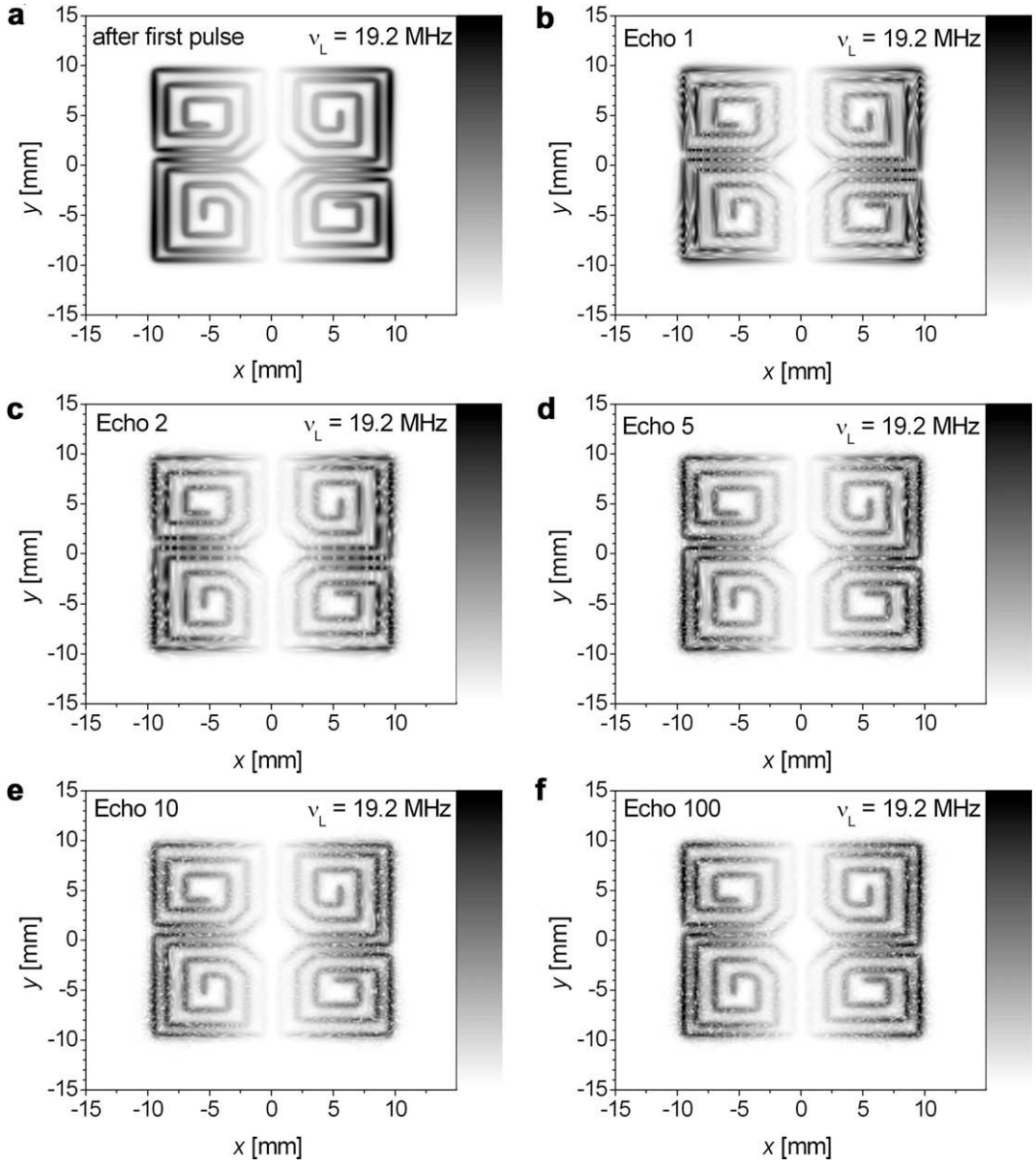

Fig. 8. Simulation of the sensitive volume of a bar magnet NMR-MOUSE® with butterfly coil in a horizontal *xy* plane after first pulse (a) and after the first Hahn echo (b). Superposition of Hahn and stimulated echoes are shown for the second (c), fifth (d), tenth (e) and hundredth (f) echoes of a CPMG pulse sequence.

The time-dependent NMR response was simulated for a CPMG pulse sequence by a variation of the C++ program used to obtain the spatial distributions of the sensitive volumes presented in Figs. 7 and 8 (Fig. 9). A general characteristic of CPMG echoes train is the fact that the first echo (a pure Hahn echo) is smaller than the subsequent echoes of the train, if one neglects relaxation effects. Another feature is the fact that the second echo is larger than the rest of them, clearly observed in Fig. 9a and b. The amplitude of the others echoes seems to be affected only by the relaxation ratios. Moreover, the CPMG decay is characterized by a very short transitory regime [19].

For a relaxation time ratio of 1 (here, $T_1 = T_2 = 25$ ms Fig. 9a) the CPMG decay follows the ideal path as shown by the drawn black line for a mono-exponential decay with $T_2 = 25$ ms passing through the echoes maxima. All three magnetization components are weighted equally and no difference to measurements in homogeneous or inhomogeneous fields are expected. Nevertheless, for a long CPMG pulse sequence with a duration compared to T_1, new z magnetization will be generated, the corresponding spins can be excited by the radiofrequency pulses and lead to a small increase of the later echo amplitudes. During all simulations relaxation over the pulse duration was neglected.

The decay of a CPMG echo train for the same T_1 value of 25 ms and a transverse relaxation time of $T_2 = 12$ ms is presented in Fig. 9b. The exponential decay curve, with $T_2 = 12$ ms and the same amplitude as in the previous figure, decays faster than the echo train. A direct consequence of the T_1 relaxation is the fact that by fitting the echo decay, an apparent transverse time $T_{2,\mathrm{eff}}$ larger than T_2 is obtained. This effect is increasing at larger T_1/T_2 ratios as is presented in Fig. 9c for $T_1 = 25$ ms and $T_2 = 2$ ms.

3.9. Correction factor $T_2/T_{2,eff}$

We have performed a study of the effect of T_1 relaxation on the CPMG echo train decay for different T_1/T_2 ratios. For that, we have considered the maximum of the CPMG echo train simulated for well defined T_1 and T_2 input values, and fitted the resultant decay

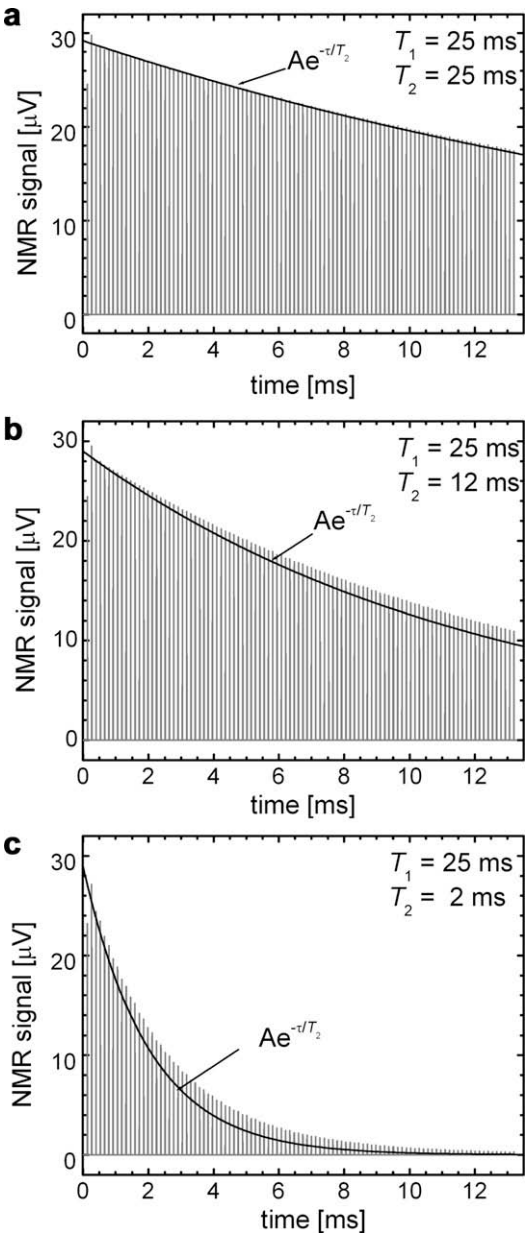

Fig. 9. Echo trains decay simulated with a C++ program for a CPMG pulse sequence for a bar magnet NMR-MOUSE® with a butterfly coil operating at a ν_L = 19.2 MHz. The responses of an isolated spin system with T_1 = 25 ms and (a) T_2 = 25 ms, (b) T_2 = 12 ms, (c) T_2 = 2 ms were simulated, and a mono-exponential decays (solid lines) characterized by the same values of the T_2 parameter are shown.

with a single-exponential curve, excepting the first two transitory echoes. The result of this fit is the $T_{2,\text{eff}}$ parameter.

Fig. 10 presents the correlation derived in the simulated CPMG decay curves for the T_1/T_2 ratio and the $T_2/T_{2,\text{eff}}$ ratio between the transverse relaxation time value used for input effective $T_{2,\text{eff}}$ value derived from the simulated CPMG response. The simulated values are represented by circles and fitted with an exponential function described by parameters with no obvious physical meaning. The $T_2/T_{2,\text{eff}}$ ratios shown in Fig. 10 are smaller than one and decrease monotonously with increasing T_1/T_2 ratio. At long values of the T_1/T_2 ratio, the curve asymptotically approaches a value of 78% of the value for $T_1 = T_2$. This particular dependence was obtained for extremely inhomogeneous magnetic fields, particular B_0 and B_1 maps and a particular T_1/T_2 ratios and echo time.

The dependence of $T_{2\text{eff}}$ on the actual T_2 and T_1 values for an NMR sensor with inhomogeneous $\vec{B}_0$ and $\vec{B}_1$ fields was reported by Hürlimann et al. [18 and reference therein]:

$$\frac{1}{T_{2,\text{eff}}} = \frac{1}{T_2} - \langle n_z^2 \rangle \left(\frac{1}{T_2} - \frac{1}{T_1} \right), \tag{26}$$

where $\langle n_z^2 \rangle$ is a normalized integral function that quantifies the inhomogeneities of the static and the radiofrequency magnetic fields. Hürlimann et al. [18] report a value of $\langle n_z^2 \rangle = 0.15$ for their sensor and a value of $\langle n_z^2 \rangle = 0.12$ for the Goelman and Prammer investigation presented in [18]. From Eq. (25) we obtain,

$$\frac{T_2}{T_{2,eff}} = 1 - \langle n_z^2 \rangle \left[1 - \left(\frac{T_1}{T_2} \right)^{-1} \right]. \tag{27}$$

The dashed line in Fig. 10 shows the dependence of the $T_2/T_{2,\text{eff}}$ ratio on T_1/T_2 according to the Eq. (26). For a value of $\langle n_z^2 \rangle = 0.18$ the agreement with the simulated $T_2/T_{2,\text{eff}}$ curve is good for small T_1/T_2 ratios. At higher T_1/T_2 ratios, the asymptotic regime is reached much earlier than by the simulated data. The value of $\langle n_z^2 \rangle = 0.18$ applies to our NMR-MOUSE sensor and is higher than the value of 0.15 reported in ref. [18]. This indicates that the NMR-MOUSE works in much more inhomogeneous magnetic fields, which is due in part to the special shape of the butterfly radiofrequency coil, and in part to the strong B_0 gradient in the depth direction.

The curves in Fig. 10 extended up to a T_1/T_2 value of 25 which is higher than what is expected in practice. Such a large value provides confidence that the fitting error is within reasonable limit for comparative types of measurements. Nevertheless, for accurate measurements in inhomogeneous fields especially for samples with similar dynamic properties described by closed values of T_2 the effect of the T_1/T_2 on the CPMG decays must be considered and eliminated. For practical applications, the $T_2/T_{2,\text{eff}}$ ratio can be employed, as an correction factor, to extract corrected relaxation times from the experimental data in order to describe the dynamical properties of the sample more accurately.

3.10. The T_1–T_2 correlation maps

The correction of $T_{2,\text{eff}}$ values to estimate the contribution of T_1 in CPMG decays measured in inhomogeneous magnetic fields can not be directly applied to relaxation time distribution obtained by Laplace inversion of relaxation decays. The main reason is that one may observe multiple values of T_1 for a well defined value of T_2

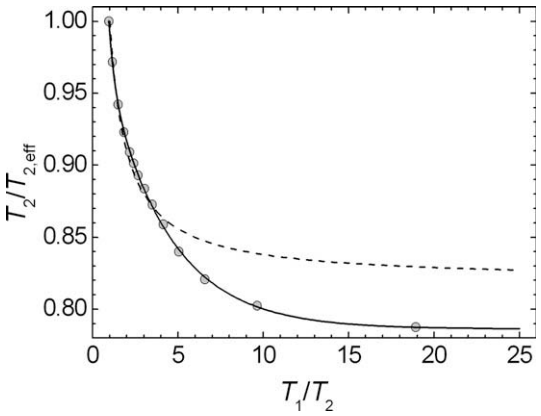

Fig. 10. The correction factor $T_2/T_{2,\text{eff}}$ as a function of the T_1/T_2 ratio for the bar magnet NMR-MOUSE® with a butterfly coil. A constant T_1 = 25 ms and a variable T_2 were the input parameters for the numerical simulation program. $T_{2,\text{eff}}$ denotes the transverse relaxation values obtained from fit the simulated CPMG echo decays with a single-exponential function. The theoretical expressions by (Eq. (26)) from reference [18] with $\langle n_z^2 \rangle = 0.18$ are identified by a dashed line.

[29,32]. To analyze this effect, a T_1–T_2 correlation map was generated by 2D Laplace inversion of data recorded with the saturation-recovery-CPMG pulse. The saturation-recovery sequence was chosen as it performs better in inhomogeneous fields than inversion-recovery sequence.

For the Laplace inversion of the NMR data we have used the fast inversion algorithm from MatLab [25–29]. The program is very flexible and allows us to receive a T_1–T_2 distribution map of 301×301 points even if in the indirect dimension there are only 100 input points. The value of the alpha regularization parameter was kept constant and set to one. Several values were tested but we found that confident results can be obtained for $\alpha = 1$. Moreover, a constant alpha value allows us to compare the T_1–T_2 distributions recorded for the same experimental conditions.

Fig. 11 shown T_1–T_2 correlation maps in terms of 2D Laplace transforms of a series of CPMG echo trains recorded for NR1 using the saturation-recovery-CPMG pulse sequence. Fig. 11a shows the 2D distribution of T_1 and T_2 values as obtained directly from the fast Laplace inversion program. The interpolation exponential function (continuous line in Fig. 10) that describes the full decay of the correction factor $T_2/T_{2,\text{eff}}$ was applied to each pixel which is characterized by well defined $T_1/T_{2,\text{eff}}$ ratio to obtain the corrected T_1–T_2 correlation map of NR1.

The T_1–T_2 distribution for NR1 is elongated perpendicular to the primary diagonal. The transverse relaxation time T_2 is distributed inversely proportional to the longitudinal relaxation time T_1. The NR1 sample is characterized by the lowest cross-link density of the series and the continuous distribution of relaxation times can be a consequence of an unclear discrimination between a liquid-like component and a solid-like component of the polymer chain network. The upper left part of the T_1–T_2 distribution touches the straight dashed line which represents equal values of transverse and longitudinal relaxation times and can characterize the liquid-like behavior of unrestricted chains such as dangling chains. From the mobile chain end toward the cross-link points the motion becomes more restricted and the transverse relaxation time is reduction. The particular T_1–T_2 distribution perpendicular to the primary diagonal indicates a relaxation mechanisms completely different from those that govern isolated spins in, for example, liquids in confined environments.

A continuous distribution of T_1–T_2 relaxation times, which cannot discern between different dynamic components of a polymer network, and cannot realistically be analyzed by a simple exponential fit of a CPMG decay with a bi-exponential function. Also a fit with a single-exponential is inappropriate as the width of distribution along T_2 dimension is large. This may explain why the data of NR1 do not fit the linear relationship of Fig. 2.

The corrected T_1–T_2 distribution functions of NR2 to NR 7 are presented in Fig. 12. A continuous distribution is observed also for NR2, but starting with NR3 and for the other sample with higher cross-link density, two components are identified. As a general feature, the distributions of relaxation times start to decrease in width along the T_2 direction with increasing cross-link density. Moreover, the gap between those two peaks is increasing on the logarithmic scale leading to increased resolution in the T_1–T_2 relaxation maps.

We expect that for this type of soft-solids the longitudinal relaxation time T_1 does not change much with cross-link density. This is underlined for samples NR2, NR5 and NR6 in Fig. 12a, d and e, respectively. A small T_1 dependence is observed for NR3 and NR7 (Fig. 12b and f) where the distribution center of the component with larger T_2 is characterized by small T_1. But as this shift is small it can be an artifact of the Laplace inversion algorithm.

This is different for NR4 (Fig. 12c), where the resultant distribution of T_1–T_2 values could be attributed to an error in the recording/processing procedure. In fact this distribution is similar with to the one observed for the NR1 sample. The distribution of relaxation times is also perpendicular to the main diagonal, shifted to smallest relaxation values and two components are observed. The question is if NR4 is a special sample or if this behavior is simply a coincidence. When analyzing previous investigations of the same sample series we find that there is a number of microscopic and macroscopic parameters sensitive to the particularities of sample NR4 like the shear modulus and the logarithmic Gaussian distribution of the correlation time, while others are not sensitive [34,35]. The NR4 sample can be considered intermediate between the sample with small cross-link and large cross-link density. It has been previously shown [34,41] that the crosslinked elastomers present a simply squared distribution on C of various microscopic parameters for low values of cross-link density. Only by considering high-order corrections of the Gaussian end-to-end vectors distribution, the full dependence of microscopic parameters on the mechanical shear modulus can be interpreted in a unified manner [34]. In this respect, the sample NR1 can be considered as the link passing from unvulcanized and uncrosslinked to vulcanized and crosslinked natural rubber.

4. Conclusions

A multi-exponential analysis of the CPMG echoes decays recorded for a series of crosslinked natural rubber samples as an example of soft solids was discussed. Since in strong inhomogeneous static and radiofrequency magnetic fields the CPMG echo train decays is weighted not only with T_2 but also with T_1, the

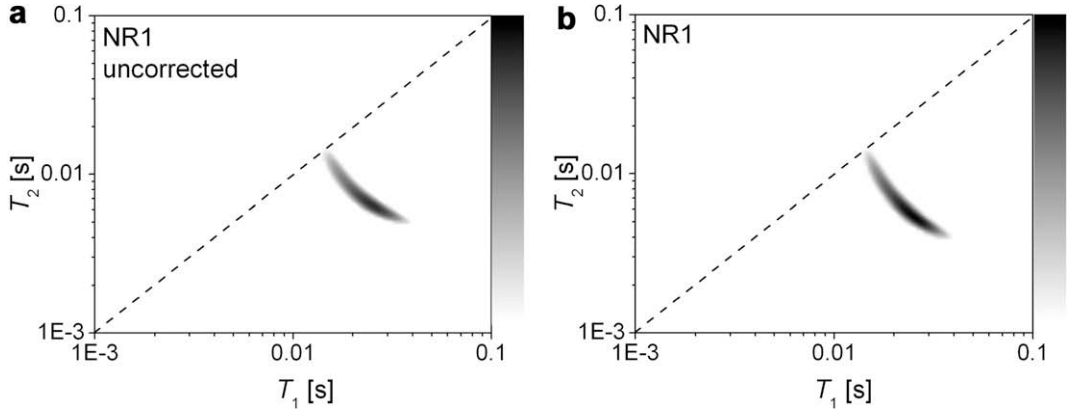

Fig. 11. Two dimensional T_1–T_2 correlation maps for the sample NR1 (a) uncorrected and (b) corrected using the correction factor $T_2/T_{2,\text{eff}}$.

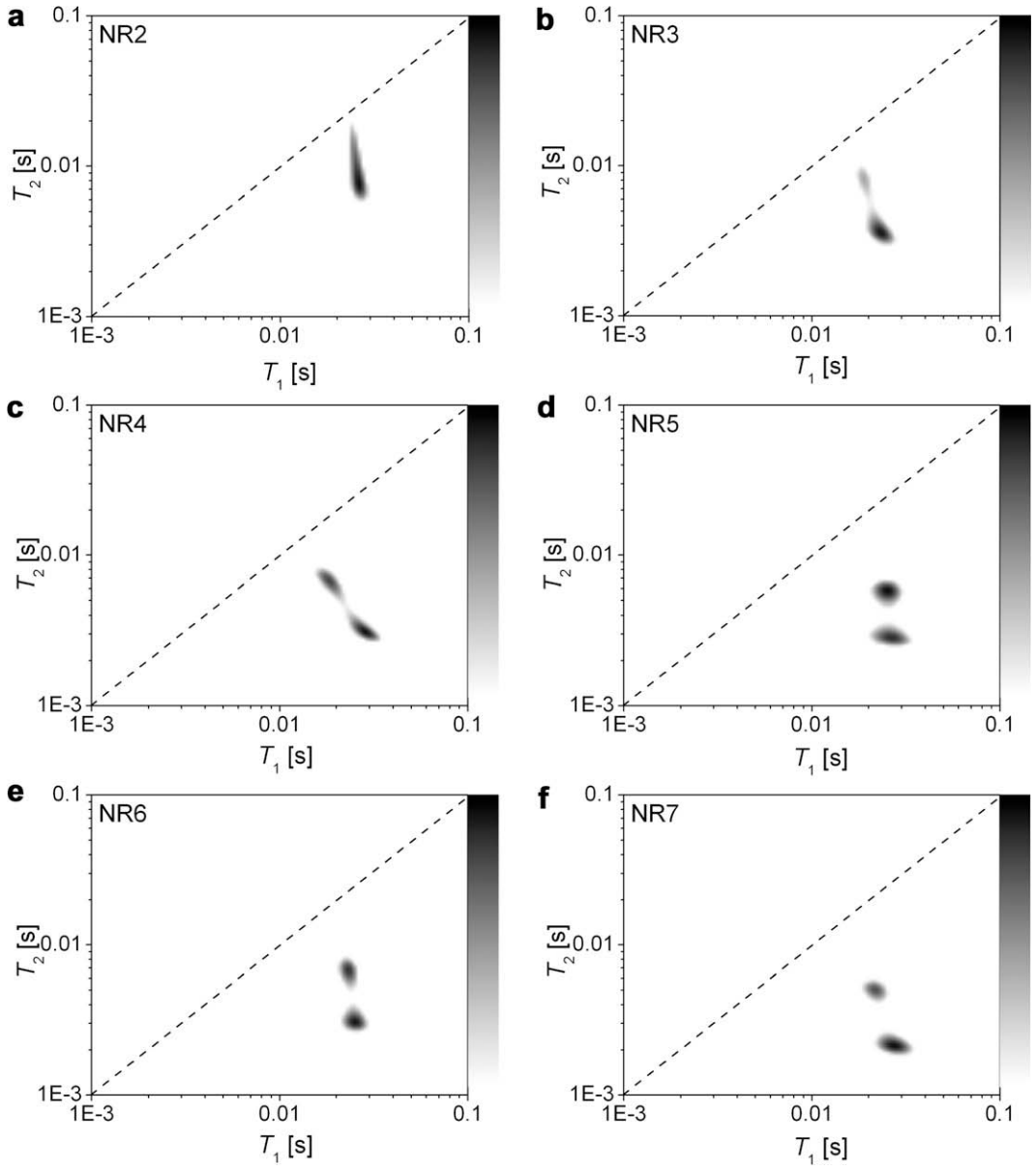

Fig. 12. Two dimensional T_1–T_2 correlation maps corrected for $T_2/T_{2,\mathrm{eff}}$ for a series of natural rubber samples with different cross-link densities. The sample are labeled (a) NR2, (b) NR3, (c) NR4, (d) NR5, (e) NR6, (f) NR7 in order of increasing cross-link density.

effect of the T_1/T_2 ratio on the $T_{2,\mathrm{eff}}$ distribution was investigated by numerical simulations. A C++ program was written to clarify this point. With the help of this program, a correction factor $T_2/T_{2,\mathrm{eff}}$, was derived. By comparison of results obtained with other devices we can conclude that the theoretical expression fits the simulated data well for T_1/T_2 ratios up to 5. The NMR-MOUSE with butterfly coil is a device with a highly inhomogeneous magnetic fields characterized by $\langle n_z^2 \rangle = 0.18$. The correction factor $T_2/T_{2,\mathrm{eff}}$ was effectively used to correct the recorded T_1–$T_{2,\mathrm{eff}}$ correlation maps for the entire series of natural rubbers samples with different crosslink densities. This procedure could be applied only to the T_1–T_2 maps, where each voxel is characterized by a well-defined value of T_1 and T_2, therefore by a well defined T_1/T_2 ratio. The effect of the T_1/T_2 ratio on the $T_{2,\mathrm{eff}}$ distribution shows an asymptotic behavior which imposes a limit of $T_{2,\mathrm{eff}}$ of 79% from the maximum of T_2 even at high T_1/T_2 ratio. It is noted that even for the sensor with the highest inhomogeneity of magnetic fields reported in this investigation and for an extreme T_1/T_2 ratio, the deviations from T_2 inflicted by measuring $T_{2,\mathrm{eff}}$ is not larger than 20%. The correction procedure can also increase the resolution in T_1–T_2 distributions maps. This will became more evident if the relevant T_1–T_2 distributions are away from the main diagonal. For example for sample NR1 one end of the T_1–T_2 distribution was near the main diagonal and was not affected while the other end away from the diagonal was shifted to smaller T_2 values. The correction procedure can produce an elongation of continuous distributions as it is the case for NR1 and NR2. Although starting with NR3 to NR7 the T_1–T_2 correlations maps present two clearly resolved peaks, a fit of the CPMG decays of NR1 and NR2 with a bi-exponential function is not justified. A general feature of the series of crosslinked natural rubber samples resulting from these correlations maps is a relatively wide distribution along the T_2 dimension and a narrow distribution along the T_1 dimension. The distribution in T_2 is mainly related to the distribution of the chain segments dynamics between the chemical and physical cross-link points.

Acknowledgement

This work was supported by a Grant of Romanian Ministry of Research and Education, CNCSIS AT 176/2006. Dan E. Demco thank also to the CNCSIS PNII 1102 grant.

References

[1] B. Blümich, J. Perlo, F. Casanova, Mobile single-sided NMR, Prog. Nucl. Magn. Reson. Spectrosc. 52 (4) (2008) 197–269.
[2] P.J. McDonald, Stray field magnetic resonance imaging, Prog. Nucl. Magn. Reson. Spectrosc. 30 (1997) 69–99. and references therein.
[3] R.L. Kleinberg, A. Sezginer, D.D. Griffin, M. Fukuhara, Novel NMR apparatus for investigating an external sample, J. Magn. Reson. 97 (1992) 466–485.
[4] G. Eidmann, R. Savelsberg, P. Blümler, B. Blümich, The NMR MOUSE, a mobile universal surface explorer, J. Magn. Reson. A 122 (1992) 104–109.
[5] B. Blümich, V. Anferov, S. Anferova, M. Klein, R. Fechete, M. Adams, F. Casanova, A simple NMR-MOUSE® with a bar magnet, Magn. Res. Eng. 15 (4) (2002) 255–261.
[6] B. Blümich, V. Anferov, S. Anferova, M. Klein, R. Fechete, A NMR-MOUSE® for analysis of thin objects, Macromol. Mater. Eng. 288 (4) (2003) 312–317.
[7] S. Anferova, V. Anferov, M. Adams, R. Fechete, G. Schröder, B. Blümich, A temperature control unit for operation with the NMR-MOUSE®: application to thermo-oxidative aging of elastomers, Appl. Magn. Reson. 27 (2005).
[8] M. Klein, R. Fechete, D.E. Demco, B. Blümich, Self-diffusion measurements by constant-relaxations method in strongly inhomogeneous magnetic fields, J. Magn. Reson. 164 (2003) 310–320.
[9] F. Balibanu, K. Hailu, K. Eymael, D.E. Demco, B. Blümich, Nuclear magnetic resonance in inhomogeneous magnetic fields, J. Magn. Reson. 145 (2000) 246–258.
[10] A. Wiesmath, C. Filip, D.E. Demco, B. Blümich, Double-quantum filtered NMR signals in inhomogeneous magnetic fields, J. Magn. Reson. 149 (2001) 258–263.
[11] A. Wiesmath, D.E. Demco, B. Blümich, NMR of multipolar spin states excited in strongly inhomogeneous magnetic fields, J. Magn. Reson. 154 (2002) 60–72.
[12] K. Hailu, R. Fechete, D.E. Demco, B. Blümich, Segmental anisotropy in strained elastomers detected with a portable NMR scanner, Solid State Nucl. Magn. Reson. 22 (2002) 327–343.
[13] R. Haken, B. Blümich, Anisotropy in tendon investigated in vivo by a portable NMR scanner, J. Magn. Reson. 144 (2000) 195–199.
[14] F. Casanova, B. Blümich, Two-dimensional imaging with a single-sided NMR probe, J. Magn. Reson. 163 (2003) 38–45.
[15] J. Perlo, F. Casanova, B. Blümich, 3D imaging with a single-sided sensor: an open tomography, J. Magn. Reson. 166 (2004) 228–235.
[16] R.L. Kleingberg, Encyclopedia of Nuclear Magnetic Resonance, vol. 8, John Wiley & Sons, 1996, pp. 4960–4969 (Chapter Well logging).
[17] G. Goelman, M.G. Prammer, The CPMG pulse sequence in strong magnetic field gradients with applications to oil-well logging, J. Magn. Reson. A 113 (1995) 11–18.
[18] M.D. Hürlimann, D.D. Griffin, Spin dynamics of Carr–Purcell–Meiboom–Gill-like sequences in grossly inhomogeneous B_0 and B_1 fields and application to NMR well logging, J. Magn. Reson. 143 (2000) 120–135.
[19] M.D. Hürlimann, Diffusion and relaxation effects in general stray field NMR experiments, J. Magn. Reson. 148 (2001) 367–378.
[20] C.A. Meriles, D. Sakellariou, H. Heise, A.J. Moulé, A. Pines, Approach to high-resolution ex situ NMR spectroscopy, Science 293 (2001) 82–85.
[21] H. Heise, D. Sakellariou, C.A. Meriles, A.J. Moulé, A. Pines, Two-dimensional high-resolution NMR spectra in matched B_0 and B_1 field gradients, J. Magn. Reson. 156 (2001) 146–151.
[22] C. Meriles, D. Sakellariou, A. Pines, Resolved magic-angle spinning of anisotropic samples in inhomogeneous fields, Chem. Phys. Lett. 358 (2002) 391–395.
[23] J. Perlo, F. Casanova, B. Blümich, Ex situ high resolution spectroscopy, Science 315 (2007) 1110–1112.
[24] M.D. Hürlimann, Encoding of diffusion and T_1 in the CPMG echo shape: single-shot D and T_1 measurements in glossy inhomogeneous fields, J. Magn. Reson. 184 (2006) 114–129.
[25] L. Venkataramanan, Y.Q. Song, M.D. Hürlimann, Solving fredholm integrals of the first kind with tensor product structure in 2 and 2.5 dimensions, IEEE Trans. Sig. Process. 50 (2002) 1017–1026.
[26] M.D. Hürlimann, L. Venkataramanan, Quantitative measurement of two-dimensional distribution functions of diffusion and relaxation in glossy inhomogeneous fields, J. Magn. Reson. 157 (2002) 31–42.
[27] Y.Q. Song, L. Venkataramanan, M.D. Hürlimann, M. Flaum, P. Frulla, C. Straley, T_1–T_2 correlation spectra obtained using a fast two-dimensional laplace inversion, J. Magn. Reson. 154 (2002) 261–268.
[28] M.D. Hürlimann, M. Flaum, L. Venkataramanan, C. Flaum, R. Freedman, G.J. Hirasaki, Diffusion-relaxation distribution functions of sedimentary rocks in different saturation ratio, Magn. Reson. Imag. 21 (2003) 305–310.
[29] M. Hürlimann, L. Burcaw, Y.Q. Song, Quantitative characterization of food products by two-dimensional D–T_2 and T_1–T_2 distribution functions in a static gradient, J. Colloid Interface Sci. 297 (2006) 303–311.
[30] S. Godefroy, P.T. Callaghan, 2D relaxation/diffusion correlations in porous media, Mag. Res. Imaging 21 (2003) 337–340.
[31] K.E. Washburn, P.T. Callaghan, Propagator resolved transverse relaxation exchange spectroscopy, J. Magn. Reson. 186 (2007) 337–340.
[32] N. Marigheto, L. Venturi, D. Hibberd, K.M. Wright, G. Ferrante, B.P. Hills, Methods for peak assignment in low-resolution multidimensional NMR cross-correlation relaxometry, J. Magn. Reson. 186 (2007) 327–342.
[33] L. Monteilhet, J.P. Korb, J. Mitchell, P.J. McDonald, Observation of exchange of micropore water in cement pastes by two-dimensional T_2–T_2 nuclear magnetic resonance relaxometry, Phys. Rev. Lett. E 74 (2006) 061404.
[34] R. Fechete, D.E. Demco, B. Blümich, Chain orientation and slow dynamics in elastomers by mixed Magic-Hahn echo decays, J. Chem. Phys. 118 (5) (2003) 2411–2421.
[35] D.E. Demco, R. Fechete, B. Blümich, Residual van Vleck moments in elastomers by accordion magic sandwich, Chem. Phys. Lett. 375 (2003) 406–412.
[36] R. Fechete, D.E. Demco, B. Blümich, Segmental anisotropy in strained elastomers by ^{1}H NMR of multipolar spin states, Macromolecules 35 (2002) 6083–6085.
[37] R. Fechete, D.E. Demco, B. Blümich, Enhanced sensitivity to residual dipolar couplings by high-order multiple-quantum NMR, J. Magn. Reson. 169 (2004) 19–26.
[38] R. Fechete, D.E. Demco, B. Blümich, Self-diffusion anisotropy of small penetrants in compressed elastomers, Macromolecules 36 (2003) 7155–7157.
[39] G.C. Borgia, R.J.S. Brown, P. Fantazzini, Uniform-penalty inversion of multiexponential decay data, J. Magn. Reson. 132 (1998) 65–77.
[40] M. McCraig, Permanent Magnets in Theory and Practice, Pentech Press, London, 1977.
[41] R. Kimmich, E. Fischer, P. Callaghan, N. Fatkullin, The dipolar-correlation effect on the stimulated echo. Application to polymer melts, J. Magn. Reson. A 117 (1995) 53.